

Compressible and Electrically Conducting Fibers for Large-Area Sensing of Pressures

Andreas Leber, Alexis Gérald Page, Dong Yan, Yunpeng Qu, Shahrzad Shadman, Pedro Reis, and Fabien Sorin*

Flexible pressure sensors offer a wide application range in health monitoring and human–machine interaction. However, their implementation in functional textiles and wearable electronics is limited because existing devices are usually small, 0D elements, and pressure localization is only achieved through arrays of numerous sensors. Fiber-based solutions are easier to integrate and electrically address, yet still suffer from limited performance and functionality. An asymmetric cross-sectional design of compressible multimaterial fibers is demonstrated for the detection, quantification, and localization of kPa-scale pressures over m²-size surfaces. The scalable thermal drawing technique is employed to coprocess polymer composite electrodes within a soft thermoplastic elastomer support into long fibers with customizable architectures. Thanks to advanced mechanical analysis, the fiber microstructure can be tailored to respond in a predictable and reversible fashion to different pressure ranges and locations. The functionalization of large, flexible surfaces with the 1D sensors is demonstrated by measuring pressures on a gymnastic mat for the monitoring of body position, posture, and motion.

because the surfaces to be functionalized are large and relevant pressures ranges are low.

In recent efforts, the coupling of conductive nanomaterials, including metal nanowires^[9,10] and carbon nanotubes,^[11–15] with soft materials, such as polydimethylsiloxane^[13,15] or cotton fabric,^[14] has led to a multitude of micro-electromechanical devices that are conformable and flexible. Pressure sensing with these deformable material constructs is typically achieved through changes in resistance,^[9,13–15] capacitance,^[11,12] piezoelectricity,^[16] or triboelectricity.^[10] Often with the help of microstructuring^[12,13,15] excellent sensitivities, low detection limits, and large measurable ranges were achieved. However, presented prototypes remain at a small scale—generally a few square centimeters of surface area—that hinders the integration in large fabrics or skins. Moreover,

1. Introduction


Pressure sensing plays a key role in the current technological advancement of functional soft surfaces and textiles with applications in health care,^[1–4] sports,^[5,6] and human–machine interaction.^[7,8] In particular, the measurement of pressures exerted by the human body on surfaces, such as seats or beds, represents an important benefit to health monitoring, as it can contribute to the prevention of pressure ulcers and the surveillance of motion patterns during sleep or physical exercise of patients. However, besides secondary requirements such as robust, long-term functioning, washability, and low cost, the design of integrated textile pressure sensors is challenging

the devices consist of 0D sensing elements, i.e., point sensors without spatial resolution, for which pressure localization can only be achieved through arrays of discrete sensors. Such systems necessitate numerous electrical contacts and wires within the area exposed to pressures, which are particularly susceptible to failure in flexible substrates, as well as extensive data collection and processing.

In contrast to standard 0D devices, functional fibers represent an advantageous alternative strategy toward large-area pressure detection and localization, because they are typically fabricated in large lengths, can be seamlessly integrated into textiles and, most importantly, enable distributed sensing.^[17] With the proper design, they can enable the functionalization of large areas with a drastically reduced number of required electrical connections or optical coupling placed outside the area of interest,^[18–20] leading to improved robustness and reduced manufacturing costs. Particularly promising are fibers originating from the thermal drawing process because this technique allows the simultaneous processing of conductive and insulating materials into fibers of extended lengths, fine architectures, and sophisticated functions, including pressure sensing.^[21–24] Thus far however, fiber designs with conducting polymer composites were limited to simple symmetric designs which prevented the simultaneous detection of pressure location and pressure level. Moreover, the in-depth understanding and modeling of the mechanical deformation of soft

A. Leber, Dr. A. G. Page, Dr. Y. Qu, S. Shadman, Prof. F. Sorin
Institute of Materials
École Polytechnique Fédérale de Lausanne
1015 Lausanne, Switzerland
E-mail: fabien.sorin@epfl.ch

Dr. D. Yan, Prof. P. Reis
Institute of Mechanical Engineering
École Polytechnique Fédérale de Lausanne
1015 Lausanne, Switzerland

 The ORCID identification number(s) for the author(s) of this article can be found under <https://doi.org/10.1002/adfm.201904274>.

DOI: 10.1002/adfm.201904274

multimaterial constructs, which are essential to control pressure sensing functionalities, remain to be developed. As a result, the integration of such smart fiber assemblies into large-area fabrics for pressure sensing has not been demonstrated to date.

Here, we present the design and scalable manufacture of compressible and conductive fibers, which can detect, quantify, and locate mechanical pressures along their entire lengths. The thermally drawn fibers are constituted of polymer composite electrodes arranged in a novel asymmetric architecture within a soft thermoplastic elastomer support. Taking advantage of the elastic structure, the fibers can be reversibly compressed, resulting in the selective contacting of electrodes within the fibers at distinct pressure levels. This experimentally demonstrated functioning of the fiber devices is supported by finite element analysis (FEA) to show the level of control and engineering of the pressure ranges and sensitivity that can be achieved through application-targeted fiber structures. Using only simple resistance measurements, kPa-scale pressures applied on the meter-long fibers are both reliably quantified and located. This enables the facile functionalization of large surfaces without the need of typically employed sensor arrays. Specifically, we demonstrate the potential of such fibers in large-area pressure sensing by integrating them onto a gymnastic mat for the monitoring of human body position, posture, and motion.

2. Results and Discussion

2.1. Fabrication of Compressible and Conducting Fibers

The thermal drawing technique is ideally suited for the coprocessing of various materials into long fibers with complex architectures. In this process, polymer granules are first hot-pressed into geometrically defined components, which are subsequently assembled and consolidated into a preform. In the quintessential final processing step, the preform is thermally drawn into a multimaterial fiber (Figure 1a). Even when composed of different materials and including an empty channel at its center, the resulting fiber maintains the same architecture as in the preform, while being much smaller in cross-sectional dimensions and larger in length. Additionally, the scalable process allows the fabrication of extended lengths of fibers in a few hours of operation (Figure 1b). We identified carbon black-loaded polyethylene (cPE) and poly[styrene-*b*-(ethylene-*co*-butylene)-*b*-styrene] (SEBS) as suitable active and substrate materials, respectively, in pressure-sensing fibers. While both materials share the processing attributes necessary for thermal drawing—high-viscosity material flow at elevated temperatures—and form an intimate interfacial bond in the fiber (Figure 1c), they exhibit vastly different sets of electrical and mechanical properties. Due to the formation of a percolated net-

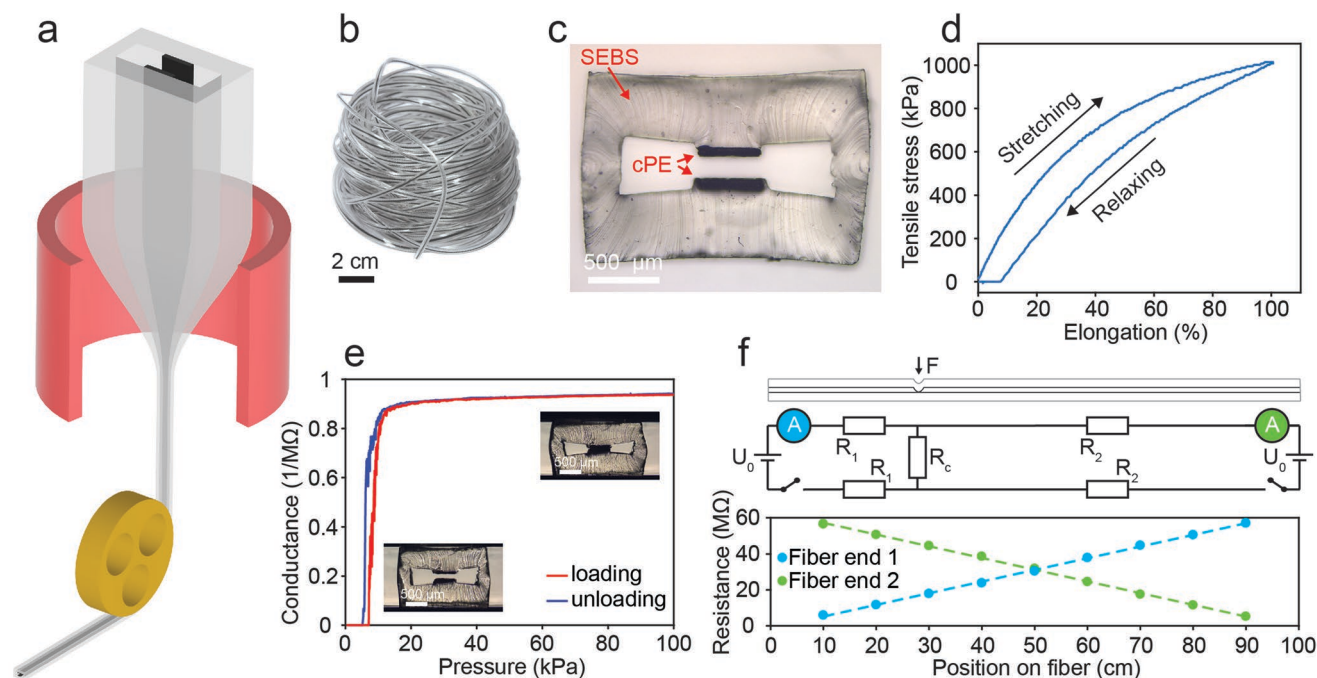


Figure 1. Materials, fabrication, and principle of operation of pressure-sensing fibers. a) Schematic of thermal drawing process for the fabrication of multimaterial fibers. b) Roll of 15 m of continuous fiber, demonstrating the scalability of thermal drawing. c) Optical micrograph of a fiber cross-section. Two conductive cPE sheets are arranged opposite to one another in a soft SEBS support structure. d) Stress–strain curve of SEBS obtained by tensile testing to 100% strain and back. The thermoplastic elastomer is soft (Young’s modulus of 2.89 ± 0.01 MPa) and nearly elastic (remnant deformation 8%). e) Compression test of the fiber while simultaneously applying a voltage between the two cPE sheets and measuring the conductance at one fiber end. The insets show optical micrographs of the fiber in the relaxed and compressed state, at which the cPE sheets are separated or in contact, respectively. f) Schematic of the fiber with a compressed section and resulting equivalent circuit. A voltage (U_0) is applied and a current is measured at either fiber end. The electrical load of the circuit is the sum of the resistances of the cPE sheets ($2 \cdot R_1$ or $2 \cdot R_2$, when considering the left or right fiber end, respectively) and the contact resistance between the two sheets (R_c). The total resistance increases linearly with the distance of the mechanical stimulation from the fiber end. Measurements from both fiber ends enable the simultaneous detection of two pressure points on the fiber.

work of conductive fillers within a thermoplastic matrix, cPE is a conductive ($\rho = 3 \text{ } \Omega\text{m}$) and rigid material. On the other hand, the thermoplastic elastomer SEBS is an insulator and exhibits large elastic deformability. To characterize the mechanical behavior of SEBS, we performed tensile testing experiments on a slab of material (Figure 1d), yielding a Young's modulus of $2.89 \pm 0.01 \text{ MPa}$ in the linear regime. In these tests, the samples were strained up to 100% and subsequently released. Even after being exposed to such extreme strains, the material almost entirely recovered its original shape during unloading. A remnant deformation of 8% when the load was fully removed was the result of viscous and plastic deformation contributions. Thus, being both soft and highly elastic, SEBS is an attractive material choice in applications where large and repeated deformations under low loads are required.^[24–26]

2.2. Pressure Detection and Localization on Fibers

The particular properties of cPE and SEBS can be exploited for pressure sensing in fibers. In a first example, two parallel sheets of cPE were embedded within a SEBS support structure and drawn into a fiber (Figure 1b,c). In the relaxed state, the two exposed faces of the conductive sheets are separated by an air gap. When mechanical pressure is applied on the fiber, the SEBS structure collapses and the two cPE conductors come in contact, practically closing an electrical circuit. Upon removal of the load, the structure relaxes, reverting back to its original state. We quantified this mechanism by subjecting the fiber to a pressure ramp while simultaneously applying a voltage between the two cPE sheets and monitoring the conductance at one fiber end (Figure 1e). At a threshold pressure of 7 kPa, the conductance abruptly jumped from 0 to $0.9 \text{ M}\Omega^{-1}$. A further increase in pressure resulted in only a small increase of conductance of $0.06 \text{ M}\Omega^{-1}$, which was attributed to a variation in contact resistance. The subsequent unloading showed that the electrical response was entirely reversible with only a small hysteresis effect, quantified by a maximum pressure discrepancy of 3 kPa.

The significant and reversible electrical response makes the proposed fiber an effective approach for pressure sensing. Particularly advantageous is the soft thermoplastic elastomer fiber structure when compared to traditional thermal drawing materials, such as the thermoplastics polysulfone and poly(methyl methacrylate), as it allows the reversible compression of a fully enclosed structure and signal triggering at kPa-scale pressures, which are relevant for applications in health monitoring.^[27] The most important feature of the pressure-sensing fibers, however, is that resistance measures can be traced back to the locations where a pressure is applied on the fibers. The working principle becomes apparent when considering the equivalent circuit of the fibers (Figure 1f). The electrical load of the circuit is made up of three resistances in series: the two internal resistances of the cPE sheets and the contact resistance between the sheets. The resistance of the two cPE sheets scales with the length of the resistive element that the current must travel through. Indeed, we found a linear increase in resistance as a point pressure was applied at positions farther away from the interrogated fiber end. Evidently, this relationship is ideal for the localization of pressures on fibers. In this sensing scheme,

the sensitivity is simply the quotient of the cPE resistivity and the cross-sectional surface area of the sheets, both of which are constant for a uniform fiber, and amounted here to $0.6 \text{ M}\Omega \text{ cm}^{-1}$. The contact resistance represents an error of the sensor, which was quantified earlier by a change in conductance and can be translated to an uncertainty in position of $<1.2 \text{ mm}$ (see the Supporting Information). The error originating from fluctuations in resistance measurements for a fiber loaded at a constant pressure and position was $0.01 \text{ M}\Omega$, corresponding to 0.2 mm (Figure S1, Supporting Information). For lengths of fibers on the scale of meters, which are employed in the large-area applications considered here, these errors are negligible. Changes in resistance readings induced by environmental factors, including temperature, strain, and humidity, which can result in more significant errors in localization, are discussed in Section 2.4. Note that the fiber sensors are truly distributed sensors that can respond to pressure with such resolution at any point along their entire length. Finally, the capability of the sensor can be extended by applying a potential and measuring a resistance alternately from either fiber end. With this technique, two pressure points can be simultaneously detected and located on the fibers.^[23]

2.3. Sensing of Pressure Level with Customizable Multielectrode Fiber Architectures

Having devised a technique to detect kPa-range pressures applied on meter-long fibers, we now turn to the challenge of simultaneously locating and quantifying a pressure event beyond a simple binary output. To address this task, we developed an alternative fiber architecture, while employing the same materials used above (Figure 2a). In this modified design, three small cPE sheets of width $200 \text{ }\mu\text{m}$ were arranged opposite to a large cPE sheet of width $1300 \text{ }\mu\text{m}$ set on an incline. The mechanical behavior of the fibers was once more investigated by applying a pressure ramp (Figure 2b). As the compressive load was increased, the top electrodes came into consecutive contact with the inclined bottom electrode, each contact event triggering an individual electrical signal at a distinct pressure level. Also in this configuration, an abrupt increase in conductance was followed by a negligible further change at increasing pressures. Presumably due to the larger deformations in the structure compared to the fiber structure presented above, a more pronounced hysteresis in the loading and unloading paths resulted in a maximum deviation of 15 kPa between the trigger and release pressures. Remarkably, each electrode retained its dependency on the location of the applied pressure (Figure 2c). Similarly to the previous fiber example, the interrogation from both fiber ends enables the localization of two pressure points along the fiber for a given top electrode-ground electrode combination (i.e., pressure level). Thus, in the current design of a fiber with three top electrodes, a total of six pressure points can be resolved. A limitation in this localization scheme is that points of higher pressure must be distanced further from the interrogated fiber ends than points of lower pressure. However, in most load settings, such as a body on a surface, the highest pressure is generated at the center and decreases toward the extremities, and the fibers can thus be employed unrestrictedly.

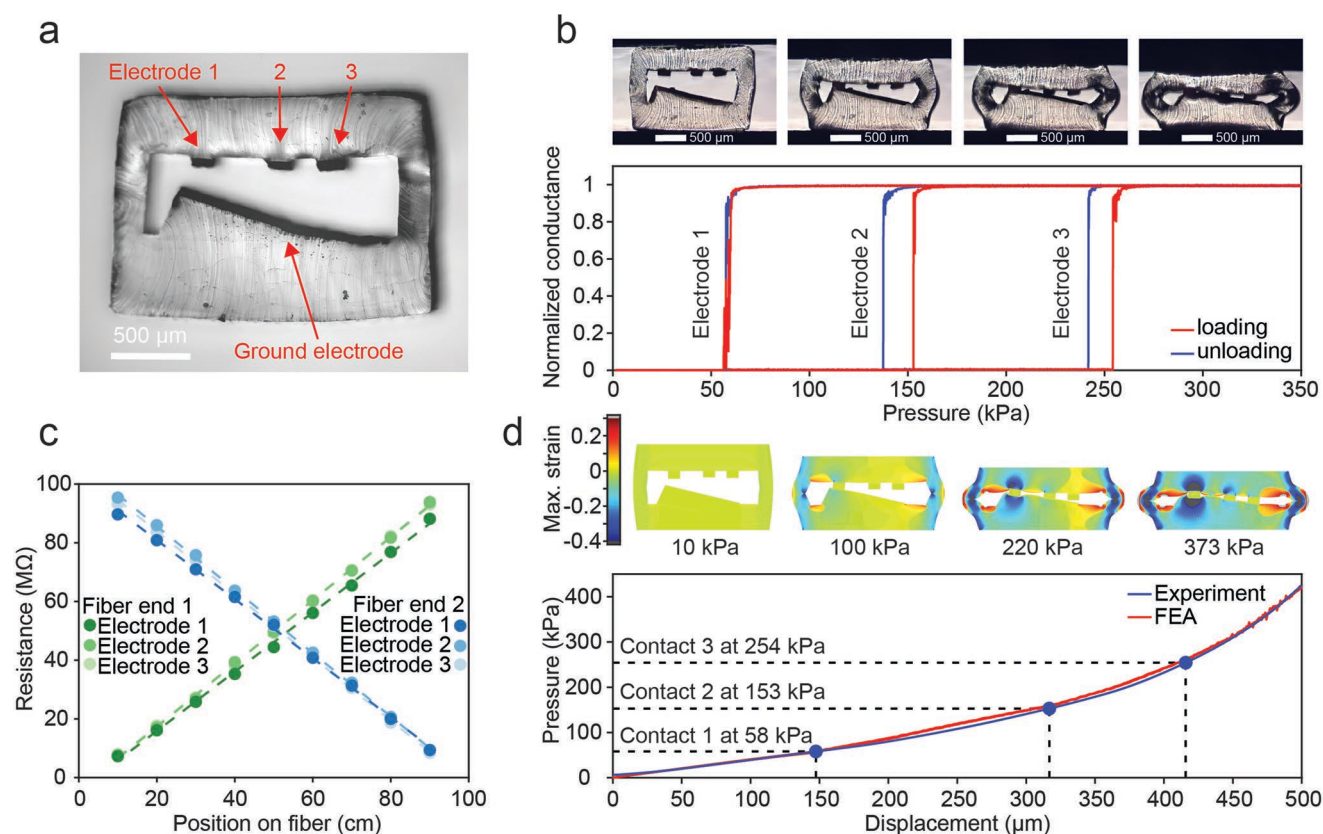


Figure 2. Fibers for detection of pressure level and location. a) Optical micrograph of the fiber cross-section. Three small conductive cPE sheets are arranged opposite to a large inclined sheet in an SEBS support structure. b) Optical micrographs of the fiber cross-section under increasing pressure. The consecutive contact of the electrodes results in an abrupt increase in the corresponding conductance at distinct pressure levels. c) Resistance of the electrode pairs as a function of the position of the pressure on the fiber. The measurement can be performed at either fiber end. Due to overlapping data points, the graph is shown once more separately for each electrode pair in Figure S2 in the Supporting Information. d) Finite element analysis of the deformation of the fiber cross-section under increasing pressure, showing the maximum principal logarithmic strain field ϵ_1 ($|\epsilon_1| \geq |\epsilon_2| \geq |\epsilon_3|$, where ϵ_1 , ϵ_2 , and ϵ_3 are the three principal logarithmic strains) in the structure at different pressure levels and the pressure on the fiber structure as a function of displacement. The progressive collapse of the structure is divided into distinct regimes separated by the consecutive contact events of the electrodes. Each additional contact results in an increase in stiffness of the fiber structure.

To further explore the mechanism underlying this mechanically induced signal triggering, we performed an FEA of the fiber structure using Abaqus/Explicit. The simulation was evaluated by comparing the mechanical response of the compressed fiber structure obtained through experimentation and the FEA, and an excellent agreement was found (Figure 2d). The FEA results indicate that the mechanical behavior of the fibers can be divided into four distinct regimes, each separated by the consecutive contact events of the electrodes. i) At low pressures, the entire applied load is carried by the two side walls of the open channel. As the pressure is increased, the walls bend progressively, and, eventually, the first top electrode comes in contact with the ground electrode. ii) With additional loading, there is an increase of the stiffness of the fiber structure, as indicated by the slope of the pressure–displacement curve, given the combined effect of the bridge generated by contact of the first electrode and the continued bending of the side walls. Similarly, further stepwise increases in the stiffness occur during regimes (iii) and (iv), associated with the subsequent contacts of the second and third electrodes, respectively. Note that the maximum principal logarithmic strain in the structure rises

to values as high as -0.4 (the negative sign signifies that the associated strains are compressive). These large strain values highlight, once more, the necessity of employing the elastomeric material SEBS instead of common thermoplastics, which could not sustain reversibly such high levels of deformation.

The stepwise increase in stiffness of the fiber under compression justifies our choice for the positions of the three top electrodes in the selected fiber design. While one might have been tempted to space these electrodes equidistantly, such an architecture would result in unbalanced pressure levels (Figure S3, Supporting Information). With the quantitative analysis of the increasing stiffness in compression of the fiber structure, we purposely shifted the position of the second top electrode away from the first and toward the third top electrode. In this noncentered electrode fiber design, signal triggering occurred at equally spaced pressure levels. We anticipate that balanced pressure levels will be preferred for most applications because applied load ranges can be classified evenly. For this reason, all subsequent experiments were performed on fibers with three top electrodes, which are triggered at the representative pressure levels of 50, 150, and 250 kPa, noting that triggering at different pres-

sure levels could be readily achieved by adjusting the electrode spacings. Additionally, the pressure level sensitivity can be tuned through the tailoring of other geometrical aspects of the fiber cross-section, such as the wall thickness, electrode gap, and angle of the ground electrode. The fiber could also be adapted for applications where shear forces in addition to compressive loads are expected. Angled forces can shift the pressures under which the electrodes are triggered and, thus, cause pressure quantification errors. These could be reduced through changes in the fiber structure, such as a reduced electrode gap and thicker side walls. Finally, the number of pressure levels detected by the functional fibers can also be increased by the inclusion of additional electrodes in the design. For example, we fabricated and characterized a fiber with six top electrodes (Figure S4, Supporting Information). Note that this increase in pressure resolution also leads to an increase in spatial resolution of a generated pressure map, as each added electrode is accompanied by a signal specifying a pressure location. Overall, the fiber-based pressure sensors that we have developed exhibit a discrete resolution of the pressure level and offer the capability of a continuous pressure location measurement. Our design can be highly customizable toward specific applications, guided by a parametric exploration of the FEA and implemented through thermal drawing.

2.4. Performance of Pressure-Sensing Fibers

To quantitatively assess the fibers' electromechanical performance, we subjected them to repeated cycles of controlled compression and relaxation while simultaneously monitoring the conductance values corresponding to the three pressure levels. The tests revealed that the electrical response of the fibers to pressure was remarkably consistent and robust (Figure 3a). All three pressure levels were triggered and released consecutively within each pressure cycle, and no changes in the conductance profiles were observed going from one pressure cycle to the next. Even after 10 000 cycles, the electrical response remained nearly unchanged. As we envision to use the fibers for pressure-localization applications, we characterized more thoroughly the ultimate output of the fiber-based sensors: the magnitude and position of pressures on the fibers. First, we measured the pressures at which the three electrode pairs were triggered during cycle 1, 10, 100, 1000, and 10 000 (Figure 3b). Variations in trigger pressures between different fiber samples were quantified by a maximum error of ± 20 kPa during the first cycle. Additionally, fatigue resulted in a maximum decrease in mean trigger pressure of 18 kPa after 10 000 cycles. The quality of pressure magnitude measurement of the fiber-based sensor, limited by intrinsic variations and fatigue, was deemed to be satisfactory, as the calculated errors fall well below the 100 kPa difference of trigger pressure between levels. Second, we evaluated the reliability of the fiber-based sensor for determining pressure position. This was achieved by assessing the relationship between the measured position and resistance prior to the fatigue experiment (Figure S5, Supporting Information). Using this calibration curve, recorded peak resistance values for each cycle could be directly translated into position readings. During the fatigue test, we monitored the change in position reading over 10 000 cycles (Figure 3c). We found that the localization was

highly consistent, quantified by a maximum error in position reading between different fiber samples during the first cycle of ± 0.2 mm and a maximum drift of mean position reading due to the repeated deformation of 0.6 mm after 10 000 cycles.

Next, we investigated the response time of the fiber-based pressure sensors to mechanical stimuli (Figure 3d). The supported bandwidth represents an important sensor specification because human body motion can reach frequencies as high as 10 Hz.^[28] We compressed the fibers cyclically at frequencies of 1, 10, and 20 Hz, and simultaneously monitored the electrical response. Experiments at higher frequencies could not be performed due to limitations of the testing machine. Even at the highest considered frequency of 20 Hz, the fiber followed the motion of the indenter faithfully, and all three pressure levels were triggered and released within each deformation cycle, resulting in a constant signal amplitude.

We also tested the performance of the fiber-based sensors under different environmental conditions, including humidity, temperature, and strain. Proper functioning in variable environments is an advantageous device property, as the fibers could be exposed to moisture, heat, and deformations during applications involving the human body. Furthermore, practical functional textiles should be machine washable. First, we tested the fibers' stability in humid environments (Figure 3e). In this test, fibers were first calibrated and subsequently submerged in a water bath. While being submerged, the fibers were compressed at the predetermined positions and the outputs recorded after 1 and 24 h in water. A comparison of the positions determined by the fibers revealed that the exposure to water had practically no effect on the functioning of the fiber-based sensors, validating their robustness in humid environments. To investigate the effect of temperature on the functioning of the fiber-based sensors, we applied a controlled temperature ramp to the fibers while monitoring the resistance of the ground electrode end-to-end (Figure 3f). An increase in temperature from 25 to 50 °C resulted in a resistance difference per fiber length of $0.025 \text{ M}\Omega \text{ cm}^{-1}$. This increase in resistance was found to be almost entirely reversible, quantified by a remnant change in resistance per length of $0.003 \text{ M}\Omega \text{ cm}^{-1}$. While the difference in resistance induced by a change in temperature scales orders of magnitudes below the sensitivity of the pressure localization ($\approx 1 \text{ M}\Omega \text{ cm}^{-1}$), it could reduce the accuracy of the fiber-based sensor for large temperature differences and exposed fiber lengths. Thus, we tested the functioning of the fibers at an elevated temperature of 50 °C (Figure 3g). In this test, fibers were first calibrated regarding their pressure position-resistance relationship at room temperature. After heating the fibers from 25 to 50 °C, pressures were once more applied at the same predetermined positions and the resulting resistance readings directly converted using the calibration curves obtained at room temperature. Indeed, the significant temperature rise induced a non-neglectable error in the localization of pressures of up to 15 cm. However, this issue can be resolved by taking advantage of the multielectrode design of the fibers. While the pressure localization relies on the resistance measurement of electrode pairs interrogated from one fiber end, the resistance of a single electrode end-to-end can also be monitored. We used this measure to establish a temperature correction factor with which the calibration curve can be continuously

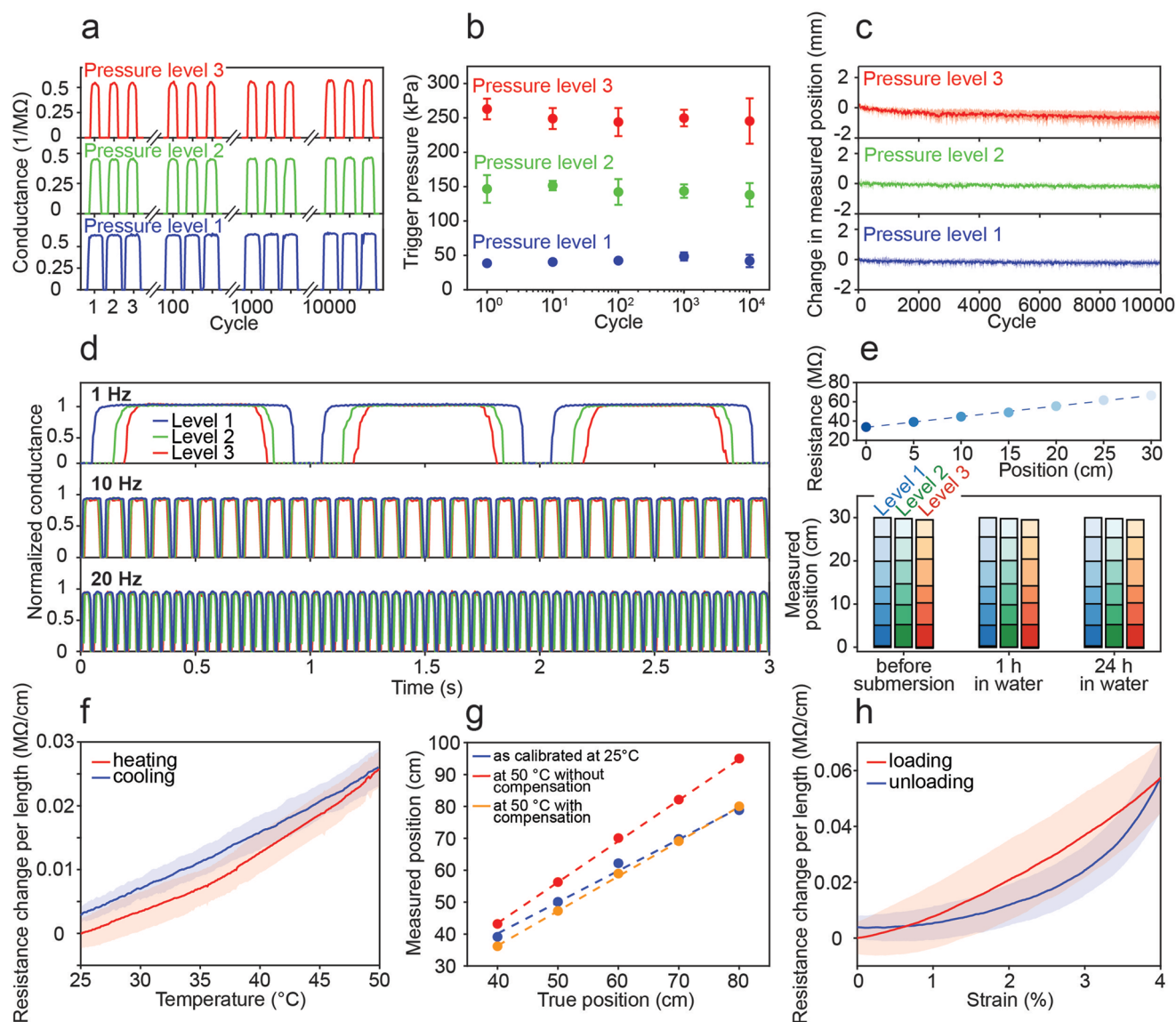


Figure 3. Performance of the pressure-sensing fibers. a) Electrical response of the three pressure level-indicating electrode pairs in the fibers under repeated compression and relaxation for 10 000 cycles. Only the conductance profiles at three consecutive cycles starting at cycle 1, 100, 1000, and 10 000 are shown. b) Change in trigger pressure of the three electrode pairs as a function of cycle number. The error bars represent the standard deviation between different fiber samples. c) Change in location reading of the three electrodes as a function of cycle number. The location is calculated using the peak conductance of previously calibrated electrode pairs for each cycle. The lines represent the mean and the shaded areas the standard deviation between different fiber samples. d) Time-resolved electrical responses of the fibers to compression at different frequencies, illustrating the bandwidth of the sensor. e) Stability of fiber-based sensors under water. The resistances of the electrodes in the fibers are linearly dependent on the position of the applied pressure, shown exemplarily only for one electrode pair. The color shade in the plot is relevant for the subsequent illustration. The positions determined using the calibrated fibers are compared in dry conditions to submersion in water for 1 and 24 h. The shade of color indicates the true position at which the fibers are compressed, and the height of the bars in the bar chart the measured position determined with the fibers. f) Change in resistance per length of the fiber ground electrode induced by an increase and subsequent decrease in temperature. The lines represent the mean and the shaded areas the standard deviation. g) Pressure position determined by the pressure-sensing fibers as a function of true position at the temperature of calibration, at an elevated temperature without compensation, and at an elevated temperature with compensation, reducing the error in pressure localization induced by the temperature effect. h) Change in resistance per length of the fiber ground electrode due to an applied and subsequently released axial strain. The lines represent the mean and the shaded areas the standard deviation.

adjusted for any given temperature (see the Supporting Information). Using this compensation scheme, the temperature-induced error could be significantly reduced to a maximum value of 3 cm and pressures localized without recalibration at elevated temperatures. The actual temperature change or even

the source of the resistance change must not be known for the compensation as long as the fiber is uniformly exposed to it. Note also that the electrode used for the monitoring of temperature-induced resistance changes must not necessarily be one involved in the pressure localization but could also be a separate

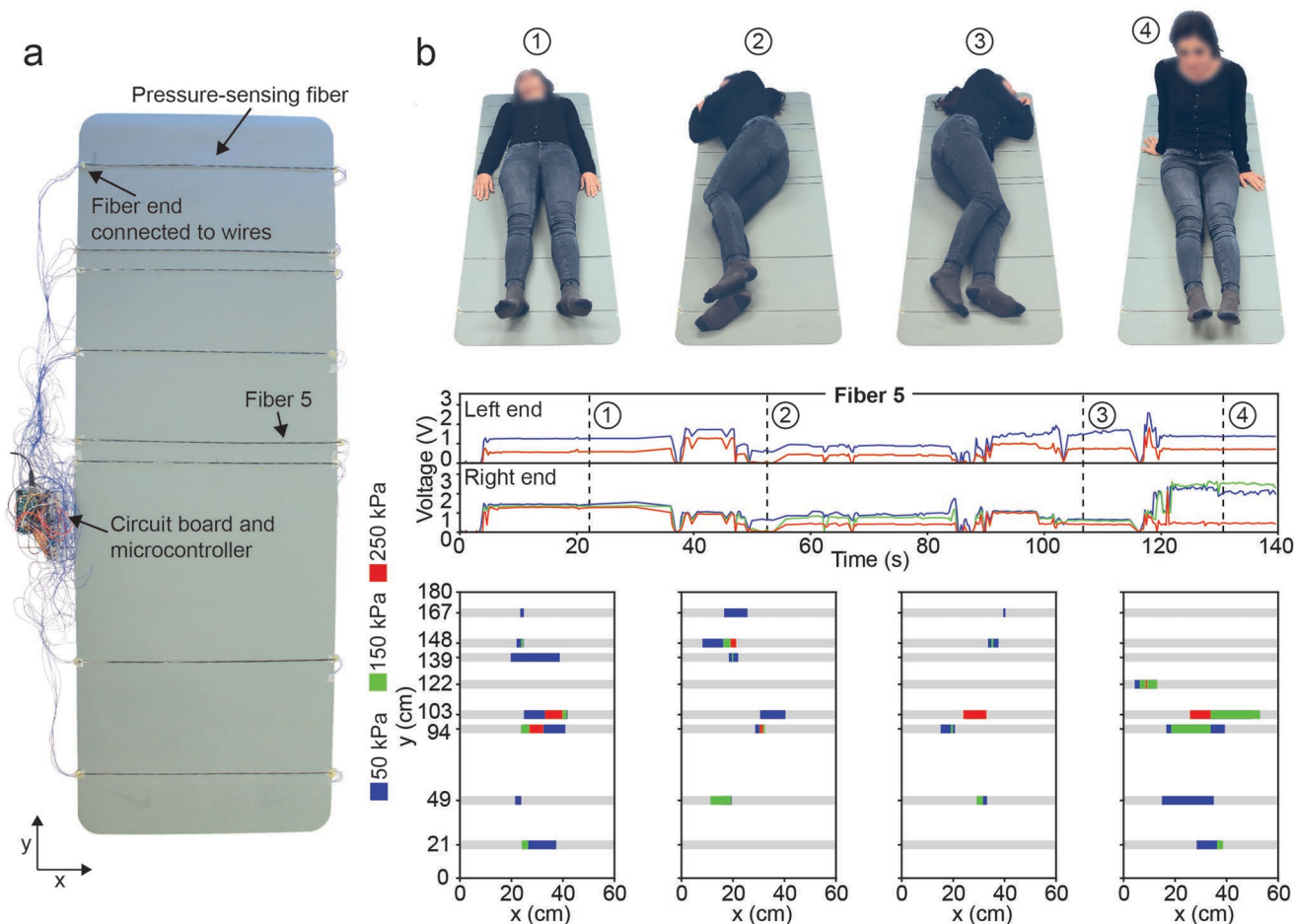


Figure 4. Fingers in human body posture and motion monitoring. a) Eight pressure-sensing fibers are integrated on a gymnastic mat. The electrodes exposed at the fiber ends are connected to a circuit board and are interrogated by a microcontroller. Fiber 5 and a coordinate system are shown, which are relevant for subsequent illustrations. b) Photographs of a volunteer lying on the gymnastic mat in different positions labeled 1 to 4. The raw outputs of fiber 5 as a function of time for the entire test, including shifts from one body position to the next, are shown as an example. The pressure level is indicated by the number of electrodes that are triggered, while the distance of the pressure position to the fiber end is quantified by the signal value. The times at which photographs were taken are indicated on the plot. Automatically generated pressure contour plots are obtained by processing the data collected by all fibers with the help of previously determined calibration curves. Displayed pressure areas are defined by the two position readings obtained for every fiber and pressure level and are thus a representation of only the pressure profile of the body.

electrode integrated within the fibers. As a final environmental stimulation, we characterized the effect of an axial strain applied along the fibers (Figure 3h). In this test, the resistance of the ground electrode end-to-end was measured while the fibers were elongated to 4% and subsequently released. While the electrode remained conductive even at elevated strain levels, a resistance difference per fiber length of up to $0.057 \text{ M}\Omega \text{ cm}^{-1}$ was found. Also in this case, the effect was reversible resulting in a remnant resistance change per length of $0.004 \text{ M}\Omega \text{ cm}^{-1}$ after unloading. As a longitudinal strain is expected to affect all electrodes uniformly, the same compensation scheme introduced for the temperature effect could be employed to reduce the error in pressure localization applications where longitudinal strains are to be expected. More complex modes of deformation, such as fiber bending, could also perturbate the correct functioning of the fiber-based sensors. However, as only applications of the fibers on flat surfaces are envisioned, the analysis bending-induced errors goes beyond the scope of this work.

2.5. Pressure-Sensing Fibers in Human Body Position, Posture, and Motion Monitoring

To demonstrate the potential of fiber assemblies in large-area pressure sensing applications, we integrated multiple fibers onto a gymnastic mat for the monitoring of body position, posture, and motion (Figure 4a). We placed eight fibers strategically on the mat at positions where the highest body pressures are expected, including the head, shoulders, tailbone, and heels. The four electrodes at each fiber end were connected to a custom circuit board using electrical wires, and a microcontroller was used to interrogate the fibers. The prototype highlights two key aspects of the fiber technology: first, the outstanding throughput of thermal drawing, even at a laboratory scale, as the fiber used to functionalize the entire surface of $180 \text{ cm} \times 60 \text{ cm}$ was obtained from a single drawing experiment; second, the number of electrical connections, which is orders of magnitude lower than what would be needed to

functionalize such a surface with 0D sensors. To directly output pressure positions during use, the fibers were calibrated before testing the device. This procedure consisted of compressing each fiber at five predetermined points and correlating the measured signals to the true positions. The performance of the calibrated device was subsequently evaluated by having a volunteer lie on the mat in different positions, and continuously recording signals generated by all fibers (Figure 4b). The signals of the sensor system, shown here only for the fifth fiber from the top as an example, proved to be stable. Signals collected from all fibers were translated to positions using the calibration curves. To make the gathered data more accessible to users, the readings were visualized in pressure contour plots that were automatically generated in real-time. In these, the displayed pressure areas are defined by the two position readings obtained for every fiber and pressure level and are thus a representation of only the pressure profile of the body. While an increase in pressure within the outer determined body profile will be detected through the triggering of another electrode pair, a decrease will not, which is a limitation of our fiber-based sensor. Nonetheless, as shown by the close correlation to the photographs of different body positions, the pressure plots can be used to determine body position, posture, and movement. Moreover, the location of an exceedance of a threshold pressure is easily picked out on the graphics. Knowledge of a critical pressure location over time is crucial in assessing the risk for the formation of bedsores.^[29] We also tested the device dynamically by asking a volunteer to walk on the mat as well as lie on it and shift between different body positions (Video S1, Supporting Information). Pressures could be resolved temporally and spatially, and body movements on the mat were accurately represented in pressure visualizations. The results suggest that the fiber-based monitoring system presented here allows for the detection of surface occupancy, assessment of body posture and kinematics, and localization of exceedance of critical pressures. In this application, we employed fibers with trigger pressures of 50, 150, and 250 kPa. However, as previously discussed, the trigger pressures can be tailored to the specific information of interest through targeted changes in the fiber geometry. Furthermore, the quality of the pressure measurement over the large area could be further improved through the inclusion of a higher number of fiber-based sensors, resulting in a larger coverage. The information obtained through the system could be particularly useful in health care, such as pressure ulcers prevention and surveillance of sleep patterns or physical exercise, but also in more general body pressure measurements, such as car seat occupancy measurements, detection of falls of elderly people, and monitoring of foot traffic.

3. Conclusion

We have developed compressible and electrically conducting fibers, optimized for the measurement of kPa-scale pressures over m²-scale surface areas. The fibers consist of conductive polymer composite electrodes arranged within a hollow, soft thermoplastic elastomer support and are fabricated by the scalable thermal drawing technique. A mechanical pressure on

the fibers results in the selective and reversible contacting of electrodes, generating an electrical signal. We showed that the fibers perform as accurate, time-responsive, and robust sensors of both pressure magnitude and location. Moreover, the fibers are customizable, as the electrical response to mechanical stimuli can be tuned through targeted changes in the architecture, enabling control of trigger pressures as well as resolution of pressure level and location. The developed fiber-based sensors stand out among standard pressure sensing strategies, such as piezoresistivity, because the discrete rather than continuous pressure level measurement is inherently impervious to noise and drift. Moreover, the fibers act as distributed sensors for the functionalization of large surface areas and enable pressure localization without the need of typically employed grids of 0D sensors, thus drastically reducing the number of failure-susceptible electrical connections. This was demonstrated by integrating the pressure-sensing fibers on a gymnastic mat, with which human body position, posture, and motion was captured. We anticipate that this robust, cost-effective, and easily implementable technology can significantly contribute to health monitoring of patients prone to pressure ulcers, and anywhere else where pressures on large surfaces need to be assessed reliably.

4. Experimental Section

Mechanical and Electrical Testing of Materials: The mechanical behavior of SEBS (Kraton) was investigated by tensile and compression testing with a standard frame (Mecmesin Multitest 2.5-i) and load cell (Mecmesin Basic Force Gauge). In tension, samples of dimensions 40 mm length, 24 mm width, and 5 mm thickness were tested and in compression samples of dimensions 20 mm length, 24 mm width, and 24 mm thickness. The displacement was set to 300 mm min⁻¹ and 1 mm min⁻¹ for tensile and compression testing, respectively. The resistivity of cPE (Goodfellow) was obtained by performing resistance measurements with an electrical testing instrument (Keithley Sourcemeter 2400) in four-probe configuration at a current of 100 μ A.

Fiber Fabrication: First, granules of the polymers were hot-pressed (Laufer Pressen UVL 5.0) into geometrically defined components. Next, the parts of different materials were assembled into a fiber preform, where a machined polytetrafluoroethene core was placed at its center to create the empty channel. The preform was consolidated in the hot press and the core was subsequently mechanically removed. Finally, the preform was drawn into a multimaterial fiber with a custom draw tower.

Structural and Electromechanical Analysis of Fibers: The cross-sections of the fibers were examined by light microscopy (Leica DM 2700 M). To investigate the fibers' electrical response to pressure, the exposed electrodes at the fiber ends were contacted using electrical wires and silver paint. Resistances were measured using the Sourcemeter at a set current of 100 nA for two-electrode fibers, and with a microcontroller (Arduino Uno) for simultaneous measurements of multiple fiber electrode pairs at an applied voltage of 5 V in a voltage divider circuit with a 10 M Ω reference resistance. In the compression test, 100 mm long fiber samples were compressed between two plates of diameter 15 mm using a dynamic mechanical analysis setup (DMA, TA Instrument DMA Q800), with which displacement and force were measured. To evaluate the correlation between pressure position and electrical response of the fibers, 1 m long fiber samples were compressed locally with a rod of diameter 5 mm. For fatigue testing, 100 mm long fiber samples were repeatedly compressed in the DMA at a frequency of 5 Hz and the conductance measured continuously for all three electrodes over 10 000 cycles. A position value

was calculated for each cycle from the peak conductance values using the previously determined calibration curves (Figure S5, Supporting Information). The same test was repeated with interruptions at cycles 1, 10, 100, 1000, and 10 000, where a controlled pressure ramp test was applied to determine the variation in trigger pressure of the electrodes. To determine the mechanical bandwidth of the fiber-based sensors, fiber samples were stimulated in the DMA at frequencies 1, 10, and 20 Hz, and the electrical response recorded with an oscilloscope (Digilent Analog Discovery) in the voltage divider circuit. To investigate the functioning of the fibers in water, 0.5 m sections of 1 m long fiber samples were submerged in a tray filled with water. The fibers were compressed locally at predetermined positions with the rod and the resistance measured with the Sourcemeter. To characterize the effect of temperature, fibers of length 1 m were placed on a hot plate and the temperature monitored with a thermocouple coupled to a multimeter (Keithley DMM7510). Pressures were applied at predetermined positions with the rod and resistance measured with the Sourcemeter. The effect of strain was assessed by elongating fibers of length 30 cm using the tensile testing stand and resistance simultaneously monitored with the Sourcemeter.

Finite Element Analysis: FEA simulations were performed using the commercial package Abaqus/Explicit, which offers a more efficient and robust convergence performance in simulations involving complex contact geometries compared to Abaqus/Standard. Given that the cross-section of the undeformed fiber is uniform along its length, the structure was simplified to a plane stress (2D) model (Figure S6, Supporting Information). Considering the nonlinear mechanical behavior of the thermoplastic elastomer used, the SEBS material was modeled by the incompressible Yeoh hyperelastic material with the strain energy potential $U = C_1(I_1 - 3) + C_2(I_1 - 3)^2 + C_3(I_1 - 3)^3$, where $I_1 = \lambda_1^2 + \lambda_2^2 + \lambda_3^2$ is the first invariant of the right Cauchy–Green deformation tensor, and λ_1 , λ_2 , and λ_3 are principal stretches. The material constants $C_1 = 482.2 \pm 1.8$ kPa, $C_2 = -82.8 \pm 2.2$ kPa, and $C_3 = 11.3 \pm 0.8$ kPa were determined by performing uniaxial tension and compression tests on SEBS. The material of the electrodes cPE was assumed to be a linear elastic material with a Young's modulus of 157 MPa determined by tensile testing (Figure S7, Supporting Information). The contact between any two surfaces (or self-contact) was assumed to be a general contact without penetration and friction. The model was discretized by $\approx 67\,000$ CPS4R plane-stress elements with an element size of ≈ 6.8 μm . A mesh convergence study was performed to ensure that the element size was sufficiently fine. Geometric nonlinearities were taken into consideration in the simulation. During loading, the bottom face of the fiber was clamped, and the top face was compressed with a prescribed uniaxial displacement that was increased smoothly from 0 to 600 μm in 5 ms and restricted laterally. The kinetic energy was less than 0.5% of the strain energy, which indicates that the simulations captured the mechanical behavior of the fiber under quasi-static loading conditions.

Fiber-Equipped Gymnastic Mat Manufacture: A fiber obtained from a single draw was cut into eight pieces, each with a length of 0.6 m. The exposed electrodes at each fiber end were contacted with silver paint and electrical wires. Next, the fibers were fixed on the gymnastic mat using double-sided tape. The wires originating from all the fibers were connected to a custom circuit board. Each set of two electrodes was connected in series to a reference resistance of 10 M Ω , forming a voltage divider. The fibers were interrogated with a microcontroller (Arduino Mega 2560) by applying a voltage of 5 V successively at each fiber top electrode and measuring the voltage across the reference resistance, which is inversely proportional to the fiber resistance. In this setup, 48 values were recorded at a rate of 4 Hz. Each fiber was calibrated by applying a point pressure at five positions. For each electrode set, the voltage level was directly correlated to a position using a two-term exponential fit.

Supporting Information

Supporting Information is available from the Wiley Online Library or from the author.

Acknowledgements

The authors thank Adrien Demongeot for his support with DMA testing. The authors acknowledge Kraton Polymers for providing the material SEBS. The authors also acknowledge the European Research Council (ERC Starting Grant 679211 "FLOWTONICS") for funding this project.

Conflict of Interest

The authors declare no conflict of interest.

Keywords

health monitoring, large-area pressure sensing, multimaterial fibers, soft materials, thermal drawing

Received: May 28, 2019
Revised: September 14, 2019
Published online: October 29, 2019

- [1] M. Nishiyama, M. Miyamoto, K. Watanabe, *J. Biomed. Opt.* **2011**, *16*, 017002.
- [2] J. K. Abraham, S. Sullivan, S. Ranganathan, in *2011 Annu. Int. Conf. IEEE Eng. Med. Biol. Soc.*, IEEE, Piscataway, NJ **2011**, pp. 4745–4748.
- [3] W. Xu, M. C. Huang, N. Amini, L. He, M. Sarrafzadeh, *IEEE Sens. J.* **2013**, *13*, 3926.
- [4] J. J. Liu, M. C. Huang, W. Xu, X. Zhang, L. Stevens, N. Alshurafa, M. Sarrafzadeh, *IEEE J. Biomed. Health Inf.* **2015**, *19*, 1682.
- [5] O. Costilla-Reyes, P. Scully, K. B. Ozanyan, *IEEE Sens.* **2015**, *16*, 1.
- [6] T. Holleczer, A. Ru, H. Harms, G. Tro, in *2010 IEEE Sens.*, IEEE, Piscataway, NJ **2010**, pp. 732–737.
- [7] A. Levi, M. Piovaneli, S. Furlan, B. Mazzolai, L. Beccai, *Sensors* **2013**, *13*, 6578.
- [8] Y.-L. Park, B.-R. Chen, R. J. Wood, *IEEE Sens. J.* **2012**, *12*, 2711.
- [9] S. Gong, W. Schwalb, Y. Wang, Y. Chen, Y. Tang, J. Si, B. Shirinzadeh, W. Cheng, *Nat. Commun.* **2014**, *5*, 3132.
- [10] L. Lin, Y. Xie, S. Wang, W. Wu, S. Niu, X. Wen, Z. L. Wang, *ACS Nano* **2013**, *7*, 8266.
- [11] D. J. Lipomi, M. Vosgueritchian, B. C. K. Tee, S. L. Hellstrom, J. A. Lee, C. H. Fox, Z. Bao, *Nat. Nanotechnol.* **2011**, *6*, 788.
- [12] C. M. Boutry, M. Negre, M. Jorda, O. Vardoulis, A. Chortos, O. Khatib, Z. Bao, *Sci. Rob.* **2018**, *3*, eaau6914.
- [13] J. Park, Y. Lee, J. Hong, M. Ha, Y.-D. Jung, H. Lim, S. Y. Kim, H. Ko, *ACS Nano* **2014**, *8*, 4689.
- [14] M. Liu, X. Pu, C. Jiang, T. Liu, X. Huang, L. Chen, C. Du, J. Sun, W. Hu, Z. L. Wang, *Adv. Mater.* **2017**, *29*, 1703700.
- [15] X. Wang, Y. Gu, Z. Xiong, Z. Cui, T. Zhang, *Adv. Mater.* **2014**, *26*, 1336.
- [16] Z. Chen, Z. Wang, X. Li, Y. Lin, N. Luo, M. Long, N. Zhao, J.-B. Xu, *ACS Nano* **2017**, *11*, 4507.
- [17] X. Tao, *Handbook of Smart Textiles*, Springer, Singapore **2015**.
- [18] H. Zhao, K. O'Brien, S. Li, R. F. Shepherd, *Sci. Rob.* **2016**, *1*, eaai7529.
- [19] M. Rothmaier, M. P. Luong, F. Clemens, *Sensors* **2008**, *8*, 4318.
- [20] A. Leber, B. Cholst, J. Sandt, N. Vogel, M. Kolbe, *Adv. Funct. Mater.* **2018**, *29*, 1802629.
- [21] T. Nguyen-Dang, A. C. de Luca, W. Yan, Y. Qu, A. G. Page, M. Volpi, T. Das Gupta, S. P. Lacour, F. Sorin, *Adv. Funct. Mater.* **2017**, *27*, 1605935.

- [22] W. Yan, A. Page, T. Nguyen-Dang, Y. Qu, F. Sordo, L. Wei, F. Sorin, *Adv. Mater.* **2019**, *31*, 1802348.
- [23] T. Nguyen-Dang, A. G. Page, Y. Qu, M. Volpi, W. Yan, F. Sorin, *J. Phys. D: Appl. Phys.* **2017**, *50*, 144001.
- [24] Y. Qu, T. Nguyen-Dang, A. G. Page, W. Yan, T. Das Gupta, G. M. Rotaru, R. M. Rossi, V. D. Favrod, N. Bartolomei, F. Sorin, *Adv. Mater.* **2018**, *30*, 1707251.
- [25] S. Zhu, J. So, R. Mays, S. Desai, W. R. Barnes, B. Pourdeyhi, M. D. Dickey, *Adv. Funct. Mater.* **2013**, *23*, 2308.
- [26] Y. Li, H. Shimizu, *Macromolecules* **2009**, *42*, 2587.
- [27] Y. Zang, F. Zhang, C. Di, D. Zhu, *Mater. Horiz.* **2015**, *2*, 140.
- [28] H. Zeng, Y. Zhao, H. Zeng, Y. Zhao, *Sensors* **2011**, *11*, 638.
- [29] R. M. Kenedi, J. M. Cowden, *Bed Sore Biomechanics*, The Macmillan Press, London **1976**.